

Ultrathin Polypyrrole Layers Boosting MoO₃ as Both Cathode and Anode Materials for a 2.0 V High-Voltage Aqueous Supercapacitor

Ying Liu, Yufeng Wang, Yuan Meng, Roshan Plamthottam, Weng Weei Tjiu, Chao Zhang,* and Tianxi Liu



Cite This: *ACS Appl. Mater. Interfaces* 2022, 14, 4490–4499



Read Online

ACCESS |



Metrics & More



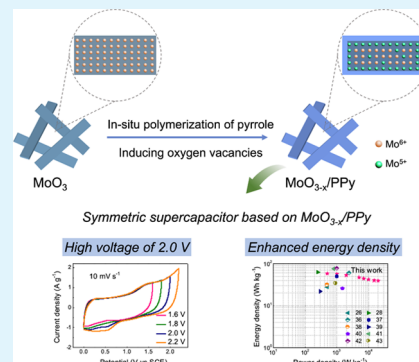
Article Recommendations



Supporting Information

ABSTRACT: An aqueous supercapacitor is an emerging energy storage unit on account of its low cost, fast energy delivery rate, and long service life. The energy density of an aqueous supercapacitor can be enlarged via extending the voltage window of electrode materials, while the aqueous electrolyte remains thermodynamically constant at 1.23 V. Herein, an aqueous supercapacitor with a 2.0 V high-voltage window is realized by core-shell MoO_{3-x}/polypyrrole (MP) nanocomposites as both cathode and anode materials. The ultrathin PPy layer on the MoO₃ core not only improves the conductivity and cycle stability of the nanocomposites but also acts as a reductant, leading to the formation of oxygen vacancies in the MoO₃ core. When used as a cathode material, the potential range of the as-obtained MP nanocomposite is up to 1.0 V. As an anode material, the stable potential range could reach -1.0 V. Due to the large potential range of the cathode and anode, the as-obtained 2.0 V aqueous supercapacitor shows a remarkably high delivery energy of 58.5 Wh kg⁻¹. The synthesis of MP nanocomposites is simple and the electrode performance is significantly enhanced; thus, it is a suitable candidate for high-energy-density aqueous supercapacitors.

KEYWORDS: polypyrrole layer, core-shell nanocomposites, oxygen vacancy, electrode materials, high-voltage aqueous supercapacitors



1. INTRODUCTION

With the rapid expansion of intelligent electronics, the demand for high-efficiency energy storage units has been significantly evoked.^{1–3} Supercapacitors, as main energy storage units, have gained great research interest on account of their abundance of essential raw materials, longevity, eco-friendliness, high power delivery rate, and high safety.^{4–7} Nevertheless, the commercial application of supercapacitors in future multifunctional electronic products is restricted by the low energy density, especially in comparison with lithium-ion batteries.⁸ The energy density (E) is decided by the working voltage (U) and the capacitance (C) since $E = 0.5 CU^2$. Therefore, it is more effective to obtain high energy density through an extension of the voltage window because E is proportional to the square of U .⁴

On the basis of different electrolytes, supercapacitors can be categorized into nonaqueous supercapacitors and aqueous supercapacitors.⁹ Nonaqueous supercapacitors, also known as organic supercapacitors, have a broad operating voltage range of 2.5–4 V, but their application prospect is bleak due to their poor ionic conductivity, high toxicity, and high price.¹⁰ Moreover, the assembly of nonaqueous supercapacitors requires an anhydrous condition, and therefore, the cost of production is high. Comparatively, aqueous electrolytes have been widely studied on account of their environmental benignity and high safety. More importantly, aqueous supercapacitors exhibit superior rate performance because an

aqueous electrolyte has a smaller ion size and higher ionic conductivity than a nonaqueous electrolyte.¹¹ However, the relatively low decomposition voltage (1.23 V) of water limits the operation voltage of aqueous supercapacitors, which correspondingly affects the energy density.¹² It has been reported that the working voltage window can be expanded via modification of the electrode materials to build a more economical supercapacitor.^{13–16} Generally, to broaden the potential window of a supercapacitor, it is necessary to increase its overpotential of the oxygen evolution reaction on the anode or the hydrogen evolution reaction on the cathode, respectively, under a steady state.^{12,13} The cathode materials must then match with the anode materials to obtain asymmetric supercapacitors. While there has been considerable success in exploring electrodes for asymmetric supercapacitors with large device voltage and storage energy, device assembly requires much more complex processes compared to that of symmetric supercapacitors due to the different types of cathode and anode electrodes. From an economical point of

Received: October 29, 2021

Accepted: December 7, 2021

Published: January 11, 2022



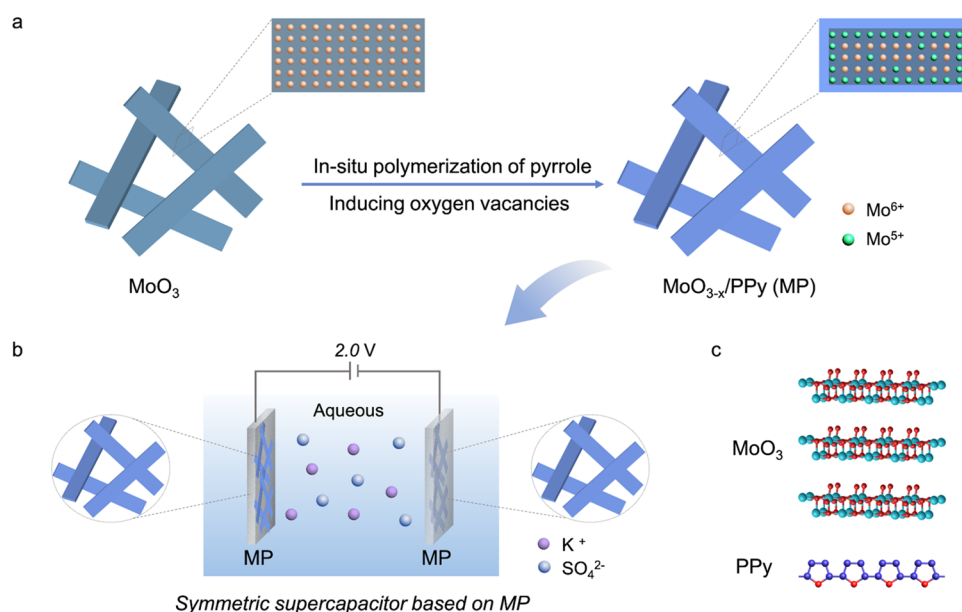


Figure 1. (a) Schematic diagram showing the preparation procedure of MP nanocomposites. During the process of pyrrole monomer oxidation polymerization on MoO_3 , MoO_3 was reduced to MoO_{3-x} and then core-shell MP was obtained. (b) Schematic illustration of the symmetric supercapacitor based on MP. (c) Chemical structures of MoO_3 and PPy.

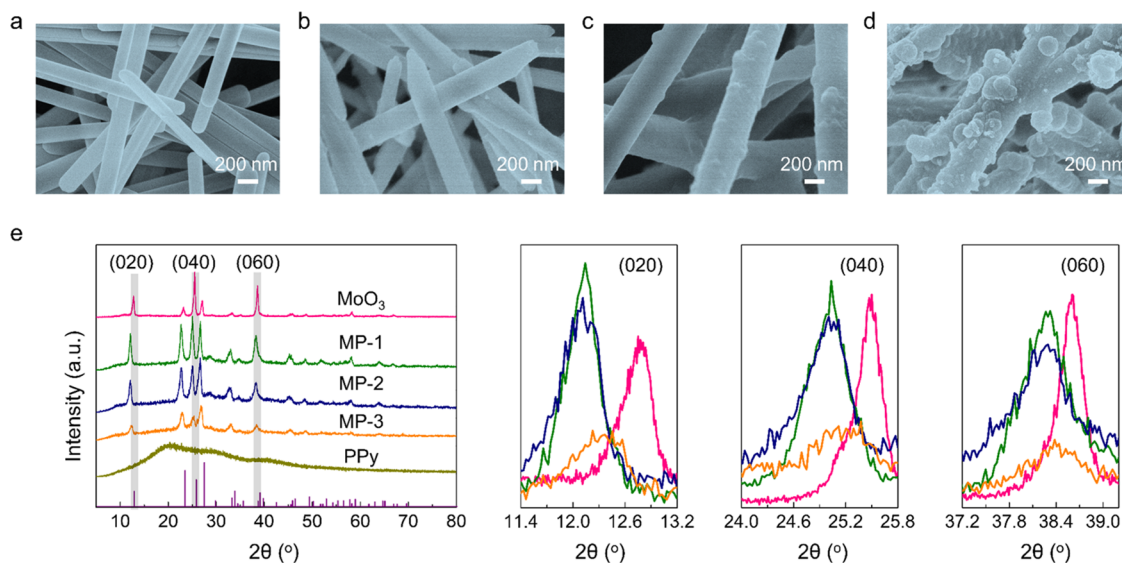


Figure 2. SEM images of (a) MoO_3 and (b–d) MP-1, -2, and -3. (e) X-ray diffraction (XRD) patterns of pristine MoO_3 , MP nanocomposites, and PPy.

view, there is a need to explore electrode materials for high-voltage symmetrical supercapacitors.

Many studies on transition-metal oxide materials as electrodes for symmetrical supercapacitors have been reported in the last decade, ranging from ZnO ,¹⁷ Fe_2O_3 ,^{18,19} V_2O_5 ,²⁰ and Co_3O_4 ²¹ to MoO_3 .^{22,23} Molybdenum trioxide (MoO_3) nanoribbons with one-dimensional (1D) structure stand out because their oxidation states are multiple, the surface-to-volume ratio is high, and 1D electron transport pathways are efficient.^{24,25} Nevertheless, its low electrical conductivity and low specific capacitance of MoO_3 impede its wide applications in supercapacitors. Intensive efforts have been devoted to coupling MoO_3 with other materials to modify its capacitive characteristics.²⁶ As a typical conducting polymer, polypyrrole (PPy) has emerged as capacitive material on account of its

high electrical conductivity, interesting redox property, ease of synthesis, and low cost.²⁷ As demonstrated in our previous work, composite materials of MoO_3 and PPy show significantly enhanced electrochemical characteristics including capacitance and cyclic stability when used as an electrode for symmetrical supercapacitors.²⁸ To our knowledge, there have been few reports on the study of MoO_3 and PPy nanocomposite materials for high-voltage symmetrical supercapacitors.

Herein, core-shell MoO_{3-x} /PPy (MP) nanocomposite electrodes are prepared for a high-voltage aqueous supercapacitor. The preparation method involves hydrothermal synthesis of MoO_3 nanoribbons and subsequently a process of pyrrole monomer oxidation polymerization on MoO_3 nanoribbons. The ultrathin PPy nanolayers on the MoO_3 core not only improve the conductivity of MoO_3 but also introduce

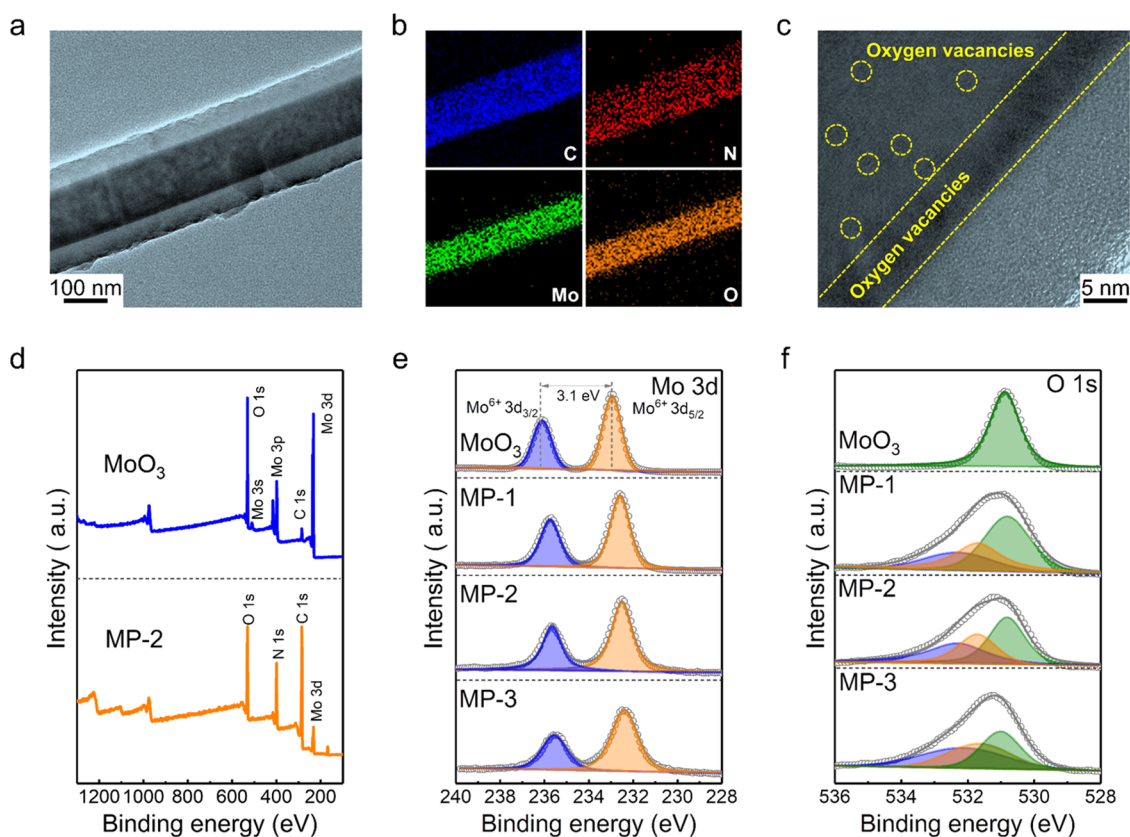


Figure 3. (a) TEM images and (b) corresponding EDX mapping images of C, N, Mo, and O elements for MP-2. (c) High resolution TEM images of MP-2 showing the existence of oxygen vacancies. (d) XPS survey spectra. XPS spectra of (e) Mo 3d and (f) O 1s.

oxygen vacancies to MoO_3 , which are both beneficial to obtaining high voltage for symmetric supercapacitors. In particular, the introduction of oxygen vacancies greatly increases the interlayer spacing and provides better conductivity, which accelerates the charge storage kinetics and improves the electrochemical activity. In addition, the outer PPy layer helps to avoid the collapse of MoO_3 nanoprisms and maintains structural stability and properties. As a consequence, when the MP is assembled into a symmetrical aqueous supercapacitor, 58.5 Wh kg^{-1} of energy density is achieved when the power density is 0.5 kW kg^{-1} because the discharging voltage window is up to 2.0 V. Moreover, the symmetrical aqueous supercapacitor employing MP as the electrode displays long-term cyclic stability, and after 10 000 cycles at 2 A g^{-1} , its capacitance retains almost 100%.

2. RESULTS AND DISCUSSION

MP nanocomposites are synthesized using pyrrole as both a reductant and a precursor for the formation of a PPy surface layer on presynthesized MoO_3 nanoprisms, and this preparation procedure of MP nanocomposites is illustrated in Figure 1. Mass ratios of MoO_3 to PPy within the MP are adjusted by tuning the initial contents of pyrrole, and the samples with increasing PPy amounts are denoted MP-1, -2, and -3, respectively. Thermal gravimetric analysis (TGA) measurements were conducted to further quantify the actual contents of PPy in the MP nanocomposites (Figure S1). Notably, the weight of neat MoO_3 remains constant over the whole temperature range below $700 \text{ }^\circ\text{C}$. However, PPy was completely consumed within this temperature range. Besides, the MP nanocomposites decompose at $\sim 245 \text{ }^\circ\text{C}$, while PPy

begins decomposing at $180 \text{ }^\circ\text{C}$, presenting its improved thermal stability. The residual weight at $700 \text{ }^\circ\text{C}$ comes from MoO_3 because it is still stable at $700 \text{ }^\circ\text{C}$, from the weight ratios of MP from TGA results. Therefore, loadings of the deposited PPy on MoO_3 within MP-1, MP-2, and MP-3 are estimated to be ~ 26.4 , 50.1 , and $62.3 \text{ wt } \%$, respectively.

Figures 2a and S2a,b show the morphologies of MoO_3 at different magnifications, which exhibit a nanoprism structure within a smooth surface. The length is up to $3\text{--}8 \text{ }\mu\text{m}$, the width is about $150\text{--}200 \text{ nm}$, and the thickness is as thin as $25\text{--}40 \text{ nm}$. The effects of PPy contents on the microstructures of MP were systematically investigated. The nanoprism structure is well maintained in the MP (Figure S3). For the MP-1 sample with the lowest PPy content, the width of the nanoprisms increases slightly compared to MoO_3 and the surface remains smooth, indicating that PPy was uniformly attached to the surface of MoO_3 nanoprisms (Figure 2b). Likewise, for the MP-2 sample with higher PPy content, the width of the whole structure increases and a small amount of PPy particles is observed on the outer surface of nanoprisms (Figure 2c). Additionally, the MP-3 sample shows that excess PPy aggregates into nanoparticles attached to the outer surface of PPy shells (Figure 2d). The thicknesses of PPy in MP-1, MP-2, and MP-3 are estimated to be ~ 13.5 , 40.8 , and 52.4 nm (Figure S4), respectively. For comparison, scanning electron microscopy (SEM) images of neat PPy exhibit aggregated morphologies of nanoparticles (Figure S5). In addition, Fourier transform infrared (FTIR) spectra of the as-synthesized samples further prove the successful composition of PPy with MoO_3 (Figure S6).

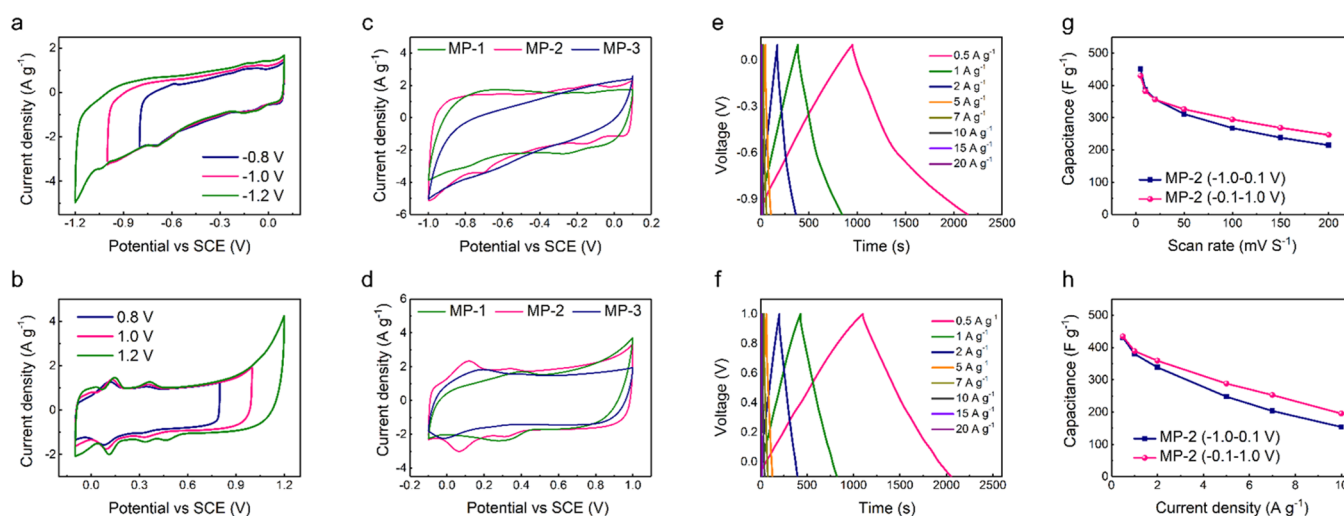


Figure 4. Electrochemical characteristics of the MP-2 electrodes in a three-electrode system: (a, b) CV curves of MP-2 as anode and cathode electrodes at 5 mV s^{-1} . (c, d) CV curves of MP-1, MP-2, and MP-3 as anode (-1.0 to 0.1 V) and cathode (-0.1 to 1.0 V) electrodes; the scan rate is 10 mV s^{-1} . (e, f) Full galvanostatic charge/discharge (GCD) curves of the MP-2 as anode (-1.0 to 0.1 V) and cathode (-0.1 to 1.0 V) electrodes; the current densities are 0.5 – 20 A g^{-1} . (g, h) Specific capacitance of MP-2 obtained from the CV and GCD curves.

Since the ultrathin layers of PPy on MoO_3 also chemically reduce MoO_3 and cause changes in the crystal structure of MoO_3 , X-ray diffraction (XRD) was subsequently conducted to provide crystalline identification of the resulting specimens (Figure 2e). MoO_3 nanoprisms are inferred to have an orthorhombic structure according to the XRD patterns (JCPDS No. 05-0508). In particular, the $(0k0, k = 2, 4, 6)$ diffraction peak intensities of neat MoO_3 nanoprisms are strong, revealing that the prepared nanoprisms own highly anisotropically grown layered crystals.²⁹ In general, the content of PPy in the samples has a great influence on the intensities and positions of the XRD peaks. The (020) , (040) , and (060) peaks, reflecting the van der Waals gap in MoO_3 , are selected to study. The peaks shift to lower angles after wrapping PPy for all three crystal plane reflections, demonstrating an increase in interplanar spacing and an expansion of the van der Waals gap, which arises from the introduction of oxygen vacancies in MoO_{3-x} .^{30,31} More specifically, the interlayer spacings of $(0k0, k = 2, 4, 6)$ crystal planes of MoO_3 , i.e., d value, are estimated to be 0.692 , 0.349 , and 0.233 nm according to the Bragg equation: $2d \sin \theta = n\lambda$, where d , θ , n , and λ are the spacing between atomic layers, the angle between the scattering plane and incident X-ray beam, an integer, and the wavelength of X-rays, respectively. The d values of MP-1 and MP-2 both increase to 0.731 , 0.356 , and 0.235 nm , and those of MP-3 increase to 0.713 , 0.353 , and 0.234 nm . It should be noticed that the three reflections hardly shift or the van der Waals gap hardly changes between MP-1 and MP-2. This may be because the introduction of PPy causes the van der Waals gap near the surface of the nanoprisms to be larger than that inside. The intensity of diffraction peaks of MP-3, however, decreases and exhibits a more disordered structure. This is attributed to the introduction of a semicrystalline nature of PPy. It was reported that an expanded van der Waals gap would significantly increase the rate performance and cyclic life of MoO_3 electrodes due to the fast ion transport in the van der Waals gap.²⁴

To further illustrate the wrapping and reduction function of PPy, transmission electron microscopy (TEM) measurements were conducted and TEM images were recorded (Figure 3a).

It clearly shows that the MP presents a core–shell structure, which corresponds to a dark MoO_{3-x} core and a PPy layer with a low contrast surrounding the core. The corresponding elemental mapping images for C, N, Mo, and O elements of MP-2 are also recorded, as shown in Figure 3b. The two elements Mo and O are distributed uniformly in the core of the nanoprisms. Elements C and N are distributed in the whole nanoprism, and these elements originate from PPy. This is indicative of successful wrapping of PPy on the surface of MoO_3 nanoprisms. Some atomic-sized pores in the core and lattice dislocations at the junction of the core and the shell are observed owing to the existence of oxygen vacancies generated by PPy coating (Figure 3c). X-ray photoelectron spectra (XPS) were then applied to shed light on the surface electronic states and chemical compositions of MoO_3 and MP nanocomposites. The existence of C, N, Mo, and O elements in MP nanocomposites is confirmed by XPS (Figure 3d). The Mo 3d XPS core spectra of the prepared MoO_3 and MP are displayed (Figure 3e). For MoO_3 , the Mo 3d XPS spectrum is made up of a spin–orbit doublet and its peaks are at 236.1 and 232.9 eV , which could be attributed to $3d_{3/2}$ and $3d_{5/2}$ of highly oxidized molybdenum cations (Mo^{6+}).³² However, the Mo 3d XPS spectrum of MP shifts to a considerably lower binding energy level without changing the energy difference ($\sim 3.1 \text{ eV}$) between the two peaks, and with an increasing pyrrole amount, and the shift increases further. The Mo $3d_{3/2}$ peaks shift to 235.8 , 235.7 , and 235.6 eV for MP-1, -2, and -3, respectively, and the peaks of Mo $3d_{5/2}$ move to 232.6 eV for MP-1, 232.5 eV for MP-2, and 232.4 eV for MP-3. Both peaks are attributed to Mo^{5+} species, suggesting the formation of oxygen vacancies.³² Figure 3f shows the O 1s spectra; for MoO_3 , the binding energy component located at $530.8 \pm 0.1 \text{ eV}$ (green curve) originates from the lattice oxygen (Oa) of MoO_3 .³³ For MP, the peak centered at $532.2 \pm 0.1 \text{ eV}$ (blue curve) is related to the chemically absorbed oxygen site (Oc).³⁴ The peak at $531.6 \pm 0.1 \text{ eV}$ (orange curve) is assigned to the oxygen vacancies (Ob) in the metal oxides.³³ Thus, combining the results of TEM and XPS, it was concluded that PPy functioned not only as a coating layer but also as a reductant to cause the formation of oxygen vacancies in MP.

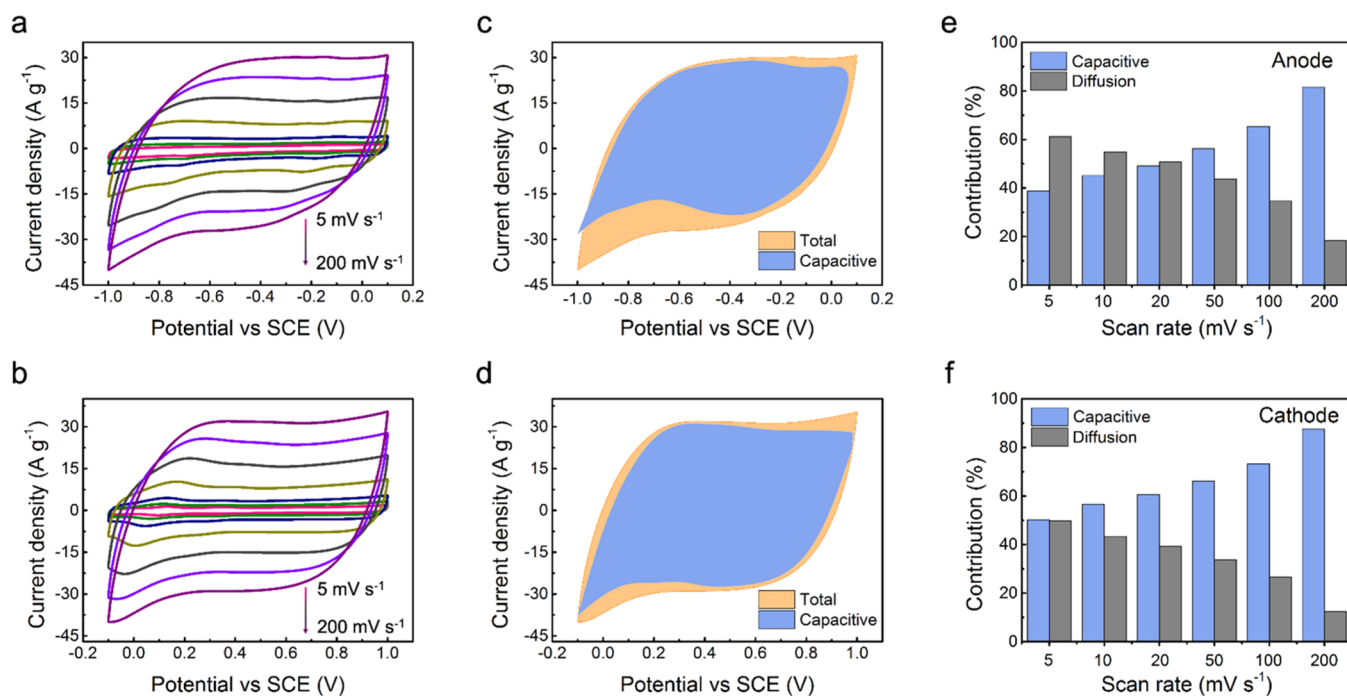


Figure 5. CV curves of MP-2 as (a) anode and (b) cathode electrodes; the scan rate is between 5 and 200 mV s^{-1} . CV curves of MP-2 as (c) anode and (d) cathode electrodes at 200 mV s^{-1} ; the capacitive contribution is represented by light blue areas. Capacitance contributions of MP-2 at various scan rates as (e) anode and (f) cathode electrodes.

To understand the electrochemical characteristics and determine the stable potential, the MP nanocomposite was tested as an anode and cathode, respectively, before evaluation of the symmetric supercapacitors. The electrodes were measured by cyclic voltammetry (CV) employing a standard three-electrode system with an aqueous 1 M K_2SO_4 electrolyte. The CV curves for the MP anode (Figure 4a) were studied, and the potential windows were set to -0.8 to 0 , -1.0 to 0 , and -1.2 to 0 V (relative to Ag/AgCl), respectively, at 5 mV s^{-1} . However, the CV for the MP cathode electrodes (Figure 4b) was performed, and the potential windows were set to 0 – 0.8 , 0 – 1.0 , and 0 – 1.2 V. For the anode, in the CV curve of -0.8 to 0 V, two pairs of redox peaks were displayed at -0.58 and -0.12 V during anode scanning and -0.69 and -0.15 V, which could be attributed to redox reactions between various Mo valence states with insertion/extraction of K^+ .²² When the upper cutoff potential was increased to -1.0 V, the position of the above two pairs of redox peaks remained unchanged, and the current density increased significantly. However, as the electrode was further operated to -1.2 V, obvious hydrogen evolution will occur. Thus, -1.0 V was adopted as the anode potential limit of the electrode. For the cathode, the CV shape was pseudocapacitive-type, showing several oxidation and reduction peaks. Apparent oxygen generation occurred when the upper cutoff potential increased to 1.2 V. Thus, 1.0 V was adopted as the cathode potential window of the electrode. MP with different PPy contents was comparatively studied for the anode and cathode, respectively (Figure 4c,d). In terms of specific capacitances at 10 mV s^{-1} , the MP-1, -2, and -3 delivered 354.8 , 387.5 , and 293.3 F g^{-1} as anodes and 311.6 , 381.8 , and 289.3 F g^{-1} as cathodes, respectively. The specific capacitance of the MP-2 electrode was obviously greater than those of MP-1 and MP-3 electrodes. The high charge storage capacity of MP-2 showed that the appropriate PPy layer thickness is critical for the improvement of the MP

nanocomposites because of the tradeoff between the electrical conductivity and diffusion path length produced by the ultrathin PPy layer. Therefore, MP-2 was determined as the sample of interest, and in the following discussion, MP referred to MP-2.

The area contained in the CV curves and the discharge time of the galvanostatic charge/discharge (GCD) curves in Figure 4e,f help in knowing the specific capacitances of the anode and cathode, respectively, and the specific capacitances of anode and cathode are plotted in Figure 4g,h. It can be seen that the anode and cathode deliver 451.1 and 430.0 F g^{-1} of specific capacitance at 5 mV s^{-1} , respectively. The anode and cathode can still maintain 47.6% (214.8 F g^{-1}) and 57.4% (246.7 F g^{-1}) of their initial value at 200 mV s^{-1} , respectively. In addition, the specific capacitance value obtained from the GCD curve is similar to that from the CV curves. For comparison, PPy and MoO_3 were also studied in an aqueous K_2SO_4 electrolyte employing the standard three-electrode system (Figures S7 and S8). The safe voltage windows of PPy as the anode and cathode are selected as -0.8 and 0.6 V, while MoO_3 as the anode and cathode are -0.6 and 0.8 V. The rate performance of MoO_3 is inferior to that of MP. The specific capacitances of MoO_3 as the anode and cathode calculated from CV curves are 182.6 and 175.0 F g^{-1} at 5 mV s^{-1} and are decreased to 51.5 and 48.7 F g^{-1} at 200 mV s^{-1} . This downward trend of the specific capacitances of MoO_3 as the anode and cathode calculated from GCD curves is similar from 5 to 10 A g^{-1} , decreased from 159.3 and 148.4 F g^{-1} to 11.3 and 23.2 F g^{-1} , respectively. Furthermore, the electrochemical impedance spectroscopy (EIS) curves reveal that the electrochemical performance of MoO_3 by in situ growth of PPy is enhanced (Figure S9). The remarkable performance of MP can be attributed to multiple reasons: (1) MoO_{3-x} provides faradic pseudocapacitance and acts as a buffer reservoir for electrolytes to shorten ion diffusion; (2) the PPy coating layer provides

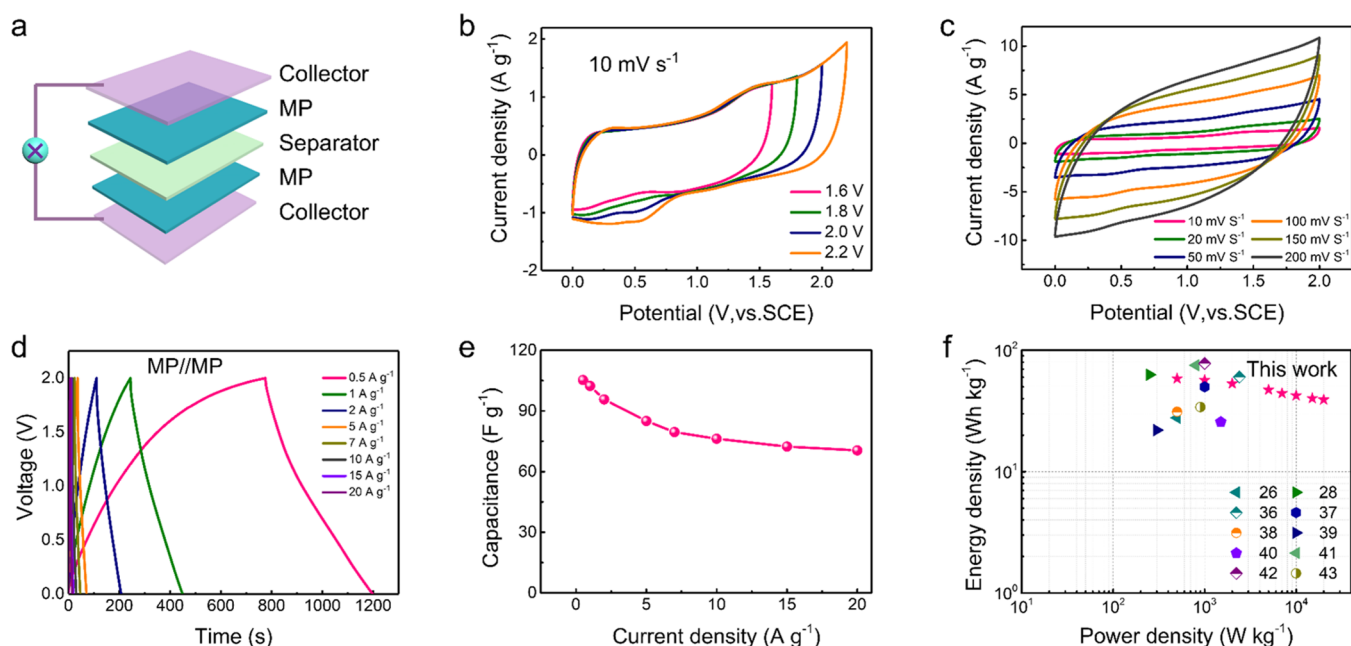


Figure 6. (a) Schematic diagram of the device using MP//MP as the electrode. (b) CV curves at a series of potential windows; the scan rate is 10 mV s^{-1} . (c) CV curves of the device with increasing scanning rates. (d) GCD curves at diverse current densities. (e) Capacitance at a series of current densities. (f) Ragone plot. The values for the reported supercapacitors using MoO_3 -based electrodes were added for comparison.^{26,28,36–43}

conductive pathways to facilitate electron transfer within the electrodes and ensures the rapid charge transfer during high-rate charging/discharging; and (3) moreover, the conductivity of the composite electrode further improves because the oxygen vacancies of MoO_3 induced by reduction of pyrrole.

To quantitatively analyze the charge storage mechanism in the electrochemical processes of MP, a kinetic study of CV curves was carried out (Figure 5). Generally, $i(V) = k_1v + k_2v^{1/2}$, where I , v , and k_1v and $k_2v^{1/2}$ represent the current at a fixed potential, the sweep rate, and the surface-controlled and diffusion-controlled capacitive contributions, respectively.¹⁶ The equation can be further transformed into $i(V)/v^{1/2} = k_1v^{1/2} + k_2$. According to the linear relationship between $i(V)/v^{1/2}$ and $v^{1/2}$ in this formula, k_1 and k_2 can be obtained. The shapes of the CV curves maintain well when the scan rate increases from 5 to 200 mV s^{-1} (Figure 5a,b), demonstrating that the rate capability is excellent and the redox reactions are highly reversible. Figure 5c,d plots the CV curve of MP as the anode and cathode at 200 mV s^{-1} based on the above formula. Typical surface-controlled capacitance contribution areas (shadowed) of the MP as the cathode and anode at 200 mV s^{-1} are observed. The ratios for the surface capacitive effect in comparison with a diffusion-controlled contribution at diverse scan rates are concluded in Figure 5e,f. The capacitance contributions of the anode and cathode increase, while the diffusion control contributions decrease as the scan rate increases. In addition, the capacitance contribution rate of the anode is always lower than that of the cathode. Since the capacitance contribution corresponds to the electric double-layer capacitance with a fast reaction speed and faradic process, the rate performance of the cathode is better. In particular, the capacitive contribution of the cathode electrode accounts for 50.2% at 5 mV s^{-1} and 87.6% at 200 mV s^{-1} , which is higher than 38.8% at 5 mV s^{-1} and 81.4% at 200 mV s^{-1} of the anode electrode. This reflects that the electrochemical kinetics of MP as cathode and anode electrodes,

especially at low scan rates, are different. The electrochemical process of the cathode electrode is mainly based on adsorption, while the anode electrode is mainly diffusion-controlled at 10 mV s^{-1} .

A symmetric aqueous supercapacitor device was further constructed to better investigate the electrochemical performance of MP. As represented in Figure 6a, the symmetric supercapacitor was assembled by employing two pieces of as-prepared MP as the electrode, $1 \text{ M K}_2\text{SO}_4$ as the electrolyte, and filter paper as the separator. The CV curves of an MP-based symmetric supercapacitor operated at a series of potential windows between 0–1.6 and 0–2.2 V at 10 mV s^{-1} are shown in Figure 6b. The device maintains a similar shape throughout the voltage window, but weak polarization occurs at 2.2 V, which means that the electrolyte decomposed. Thus, the optimal voltage window is selected at 2.0 V. The working voltage window in the neutral aqueous electrolyte is extended due to the high overpotential of dihydrogen evolution, thanks to the low concentration of hydrogen and hydroxide ions. Additionally, the high solvation energy of anions and cations provides a strong bond in the solvated shell, which prevents the decomposition of water as previously mentioned.³⁵ Furthermore, the three-dimensional (3D) interconnected structure composed of core–shell nanoprisms also increases the voltage window. The core–shell nanoprism structure with a high aspect ratio provides a lot of active centers for adsorption of H^+ , and a large interlayer spacing thus inhibits hydrogen precipitation in the electrolyte. All of the CV curves are similar to each other from 0 to 2.0 V (Figure 6c), confirming that its device has good reversibility and rate capability. To further study the capacitive behavior of the assembled symmetrical supercapacitor, GCD measurements were also performed and the current densities were set as between 0 and 2.0 V (Figure 6d). The GCD curve has a nearly symmetrical linear voltage–time relationship, showing fast charge/discharge properties and large capacitance character-

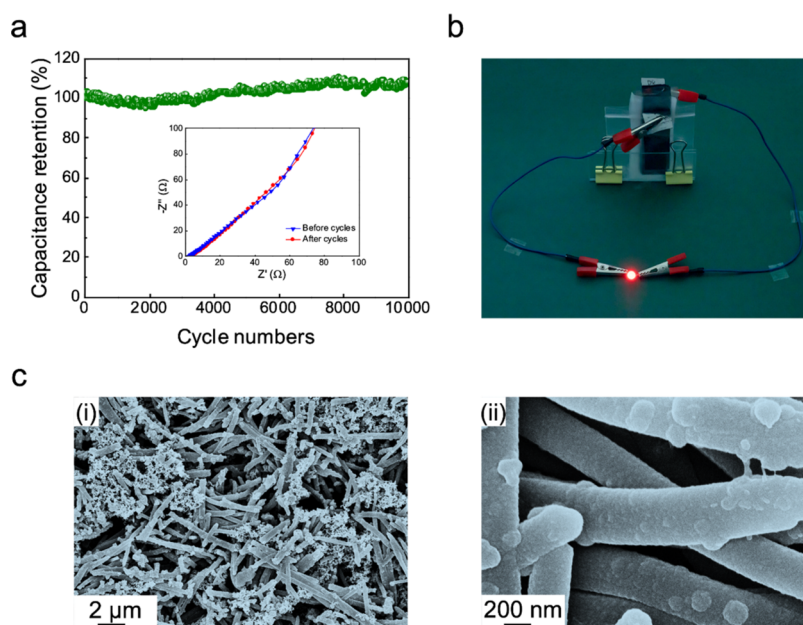


Figure 7. (a) Cycling stability at 2 A g^{-1} of MP//MP and the EIS curve (insert) before and after cycles. (b) Two symmetrical supercapacitors in series simultaneously lighting up an LED. (c) SEM images of MP electrodes after cycling measurements at (i) low and (ii) high magnifications.

Table 1. Summary of Electrochemical Parameters of MP with MoO_3 -Based Electrodes in the Literature

electrode	energy density (Wh kg^{-1})	power density (kW kg^{-1})	electrolyte	voltage (V)	reference
$\text{MoO}_3/\text{CNT} // \text{MnO}_2/\text{CNT}$	27.8	0.5	1 M Na_2SO_4	2	26
$\text{NiCo}_2\text{O}_4/\text{MnO}_2 // \text{MoO}_3/\text{PPy}$	60.4	2.4	PVA/ Na_2SO_4	1.6	41
$\text{MnO}_2/\text{MoO}_3$	50	1	1 M Na_2SO_4	2	39
$\text{MoO}_3/\text{Ti}_3\text{C}_2\text{T}_2 // \text{NAC}$	31.2	0.5	3 M H_2SO_4	1.5	43
MoO_3	22	0.3	1 M Na_2SO_4	2.2	36
$\text{MoO}_3 // \text{porous carbon}$	25.7	1.5	1 M H_2SO_4	1.4	40
3D GF-CNTs//3D GF-CNTs/ MoO_3	75.3	0.8	1 M KOH	1.6	38
MoO_3	78	1	2 M Li_2SO_4	2.0	42
h-NCS@PANI// $\text{MoO}_3 // \text{h-NCS@PANI}$	34.1	0.9	1 M H_2SO_4	1.6	37
$\text{MoO}_3/\text{PPy}/\text{PANI}$	63	0.25	0.5 M H_2SO_4	1.0	28
MP	58.5	0.5	1 M K_2SO_4	2.0	this work

istics. At the current densities of 0.5, 1, 2, 5, 7, 10, 15, and 20 A g^{-1} , the specific capacitances calculated from GCD curves are estimated to be 105.2, 102.4, 95.7, 85.0, 80.0, 76.3, 72.4, and 70.5 F g^{-1} , respectively (Figure 6e).

The energy densities at different power densities of the MP-based symmetric supercapacitor were calculated with the help of GCD curves. It is more effective to obtain high energy density through an extension of the voltage window because E is proportional to the square of U . To compare the energy storage of an MP-based electrode with the existing devices from reported works, the Ragone plots of the device with the MP-based electrode in comparison to various MoO_3 -based electrodes are demonstrated in Figure 6f. The energy density of the MP-based supercapacitor is 58.5 Wh kg^{-1} at a relatively low power density (0.5 kW kg^{-1}). Even at a power density of 20 kW kg^{-1} , the MP-based device also achieved a relatively high energy density of 39.2 Wh kg^{-1} , which is at the upper-medium level for the device using the MoO_3 -based electrodes.^{26,28,36–43} In addition, MoO_3 was assembled into a symmetric supercapacitor for comparison (Figure S10a). The CV curves of a MoO_3 -based supercapacitor operating at 10 mV s^{-1} in various potential windows (0–1.2 to 0–1.8 V) are shown in Figure S10b. With an increase of applied voltage,

the curve obviously polarized at 1.6 V. Thus, an operating voltage of 0–1.4 V for the MoO_3 -based supercapacitor is selected. The CV curves of the MoO_3 -based supercapacitor were obtained at a series of scan rates, as shown in Figure S10c, and the GCD measurements with various current densities are recorded in Figure S10d. The specific capacitances are estimated to be 80.4, 75.9, 66.5, 52.3, 45.8, 38.0, 25.9, and 18.4 F g^{-1} , corresponding to a series of applied current densities of 0.5, 1, 2, 5, 7, 10, 15, and 20 A g^{-1} , respectively (Figure S10e), assessed from the GCD curves. The rate capability of MoO_3 is inferior to that of MP. Furthermore, compared with the energy density of the MP electrode, the pure MoO_3 displayed both relatively low values at the high and low power densities (Figure S10f), suggesting its inferior energy storage ability.

Cycle stability is an important factor to be considered in the supercapacitor industry, and the cyclic stability of the MoO_3 and MP was examined at 2 A g^{-1} (Figures 7a and S10g). The MoO_3 sample experiences a serious capacitance loss, and its capacitance remains 44.1%. In comparison, the MP electrode shows significantly long-term stability, and the capacitance remains good, up to 100%, after 10 000 cycles. EIS is further performed, and the Nyquist plots of the symmetric super-

capacitor device are used to compare the effects of repeated cycles and are displayed in Figure 7a (inset). In the high-frequency regions, there is no semicircle, which is a characteristic of small charge-transfer resistance and rapid ion diffusion within MP. In the low-frequency regions, the linear behavior reveals that there is a rapid charge transfer mechanism during the charging/discharging process of the symmetrical supercapacitor device.^{44–46} After 10 000 charge–discharge cycles, only a small change in the Nyquist plot is observed, indicating its good cycle stability. This is benefiting from the favorable structure of the as-constructed MP electrode. Specifically, the PPy nanolayer on the MoO_{3-x} surface partially alleviates the volume change caused by the high-speed redox reaction. In a practical demonstration, an LED is simultaneously lighted up by two symmetrical supercapacitors in series (Figure 7b). To further observe the morphology after long-term cycling tests, SEM images collected for MoO₃ and MP electrodes after 10 000 cycles reveal that MoO₃ is severely damaged due to its structural instability from the interlayers of MoO₃ with intercalated H⁺ ions. The complete skeleton of MP remains intact with just slightly shrunk nanoprisms (Figures 7c and S10h). The strategy of using a conducting polymer layer to protect MoO₃ nanoprisms is proved successfully. Therefore, the large voltage window, high power/energy density, and good cycle stability make MP-based symmetrical supercapacitors promising for application in energy storage devices (Table 1).

3. CONCLUSIONS

In summary, the core–shell MP nanoprisms have been prepared through in situ polymerization of PPy on MoO₃ nanoprisms, and the in situ grown PPy acts as both a reductant and coating layer. The reduction of the surface of MoO₃ nanoprisms during the polymerization of PPy leads to the introduction of oxygen vacancies. Compared to conventional MoO₃-based electrodes working as only anodes, our work presents MP as both anode and cathode material. The practical symmetric MP supercapacitor allows the greatest operating voltage of 2.0 V, and its capacitance is retained well for 10 000 cycles, paving the way for high-voltage aqueous supercapacitors. This work therefore presents an alternative and effective design for high-potential electrode materials for application in aqueous supercapacitors.

4. EXPERIMENTAL PROCEDURES

4.1. Synthesis of MoO₃ Nanoprisms. MoO₃ nanoprisms were synthesized according to the hydrothermal method in previous literature.⁴⁷ About 0.30 g of NaCl dissolved in 15 mL of water and 0.60 g of Na₂MoO₄·2H₂O dissolved in 15 mL of water were mixed under stirring, and the pH value was controlled at 1 by dropwise adding 3 M HCl. The mixture solution was subsequently reacted at 180 °C in a Teflon-lined autoclave (50 mL). Upon 24 h, samples were cooled naturally, collected, washed continuously with water, and dried overnight in a vacuum.

4.2. Preparation of MP Nanocomposites. In an aqueous suspension of MoO₃ nanoprisms and the pyrrole monomer, the core–shell MP nanocomposites were synthesized through pyrrole monomer oxidation polymerization by employing APS as an oxidizer. MoO₃ nanoprisms (20 mg) were first dispersed in water (80 mL) under vigorous stirring, and pyrrole was then added to the obtained suspension under stirring at ~0 °C. APS solution (20 mL, half the moles of pyrrole) was then added. The precipitates after stirring at ~0 °C for 12 h were named MP nanocomposites. Samples added with

increasing amounts of pyrrole of 100, 200, and 400 μL are recorded as MP-1, -2, and -3, respectively.

4.3. Electrochemical Measurements. Before assembling the symmetric supercapacitor devices, the charge balance between the two electrodes needs to be considered. Thus, the mass ratio of the cathode and anode electrodes could be calculated through eq 1⁴⁸

$$\frac{m_+}{m_-} = \frac{C_- \times \Delta E_-}{C_+ \times \Delta E_+} \quad (1)$$

Here, m_+ and m_- refer to the cathode and anode electrode material masses. The specific capacitances arising from the cathode and anode electrode materials are denoted C_+ and C_- , respectively. ΔE_+ and ΔE_- are the potential windows, respectively.

The energy and power densities (E and P) of electrode materials in the constructed supercapacitors were calculated with the help of the galvanostatic charge and discharge curves, according to eqs 2 and 3, respectively⁴⁹

$$E = \frac{1}{2}C\Delta V^2 \quad (2)$$

$$P = \frac{E}{\Delta t} \quad (3)$$

Here, the specific capacitance from the two-electrode devices is expressed as C , the applied potential window is expressed as ΔV , and the discharge time is expressed as Δt .

■ ASSOCIATED CONTENT

Supporting Information

The Supporting Information is available free of charge at <https://pubs.acs.org/doi/10.1021/acsami.1c20922>.

Materials, characterizations, and electrochemical characterizations; TGA characterizations of MoO₃, MP, and PPy in air; SEM images of MoO₃ after grinding; SEM images of MoO₃ and MP at low magnifications; TEM images of MP; SEM images of neat PPy; FTIR spectra of MoO₃, MP, and PPy; electrochemical performances of the synthesized PPy and MoO₃ electrodes; EIS curves of MoO₃, MP, and PPy; schematic diagram and electrochemical characteristics of the symmetric supercapacitor employing MoO₃ as the electrode; and SEM image of MoO₃ electrode after cycling (Figures S1–S10) (PDF)

■ AUTHOR INFORMATION

Corresponding Author

Chao Zhang – State Key Laboratory for Modification of Chemical Fibers and Polymer Materials, College of Materials Science and Engineering, Donghua University, Shanghai 201620, P. R. China; orcid.org/0000-0003-1255-7183; Email: czhang@dhu.edu.cn

Authors

Ying Liu – State Key Laboratory for Modification of Chemical Fibers and Polymer Materials, College of Materials Science and Engineering, Donghua University, Shanghai 201620, P. R. China; orcid.org/0000-0001-6970-4469

Yufeng Wang – State Key Laboratory for Modification of Chemical Fibers and Polymer Materials, College of Materials Science and Engineering, Donghua University, Shanghai 201620, P. R. China

Yuan Meng – Department of Materials Science and Engineering, Henry Samueli School of Engineering and Applied Science, University of California, Los Angeles, California 90095, United States

Roshan Plamthottam – Department of Materials Science and Engineering, Henry Samueli School of Engineering and Applied Science, University of California, Los Angeles, California 90095, United States

Weng Weei Tjiu – Agency for Science, Technology and Research (A*STAR), Institute of Materials Research and Engineering, 138634, Singapore

Tianxi Liu – State Key Laboratory for Modification of Chemical Fibers and Polymer Materials, College of Materials Science and Engineering, Donghua University, Shanghai 201620, P. R. China; Key Laboratory of Synthetic and Biological Colloids, Ministry of Education, School of Chemical and Material Engineering, Jiangnan University, Wuxi 214122, P. R. China; orcid.org/0000-0002-5592-7386

Complete contact information is available at:
<https://pubs.acs.org/10.1021/acsami.1c20922>

Author Contributions

Y.L. prepared the samples, conducted the characterizations, and wrote the manuscript. Y.W. conducted the electrochemical measurements. Y.M. and R.P. performed the electrochemical analysis and wrote the manuscript. W.W.T. and T.L. reviewed and commented on the manuscript. C.Z. supervised and participated in the whole project.

Notes

The authors declare no competing financial interest.

ACKNOWLEDGMENTS

Y.L. thanks the Fundamental Research Funds for the Central Universities and Graduate Student Innovation Fund of Donghua University (Grant No. CUSF-DH-D-2019026).

REFERENCES

- (1) Mackanic, D. G.; Chang, T.-H.; Huang, Z.; Cui, Y.; Bao, Z. Stretchable Electrochemical Energy Storage Devices. *Chem. Soc. Rev.* **2020**, *49*, 4466–4495.
- (2) Fu, Y.; Zhou, H.; Hu, Z.; Yin, S.; Zhou, L. Temperature-Induced Microstructure Optimization of Co_3O_4 for the Achievement of a High-Areal-Capacity Carbon Cloth-Based Lithium Ion Battery Anode. *Compos. Commun.* **2020**, *22*, No. 100446.
- (3) Wei, W.; Tang, Q.; Liu, T.; Xia, Y.; Yan, K.; Wang, D. Preparation and Properties of Polypyrrole/Polyamide 6 Nanocomposite Film with Core-Shell Architecture for the High-Performance Flexible Supercapacitor. *Compos. Commun.* **2020**, *22*, No. 100468.
- (4) Wang, F.; Wu, X.; Yuan, X.; Liu, Z.; Zhang, Y.; Fu, L.; Zhu, Y.; Zhou, Q.; Wu, Y.; Huang, W. Latest Advances in Supercapacitors: From New Electrode Materials to Novel Device Designs. *Chem. Soc. Rev.* **2017**, *46*, 6816–6854.
- (5) Zhu, Q.; Zhao, D.; Cheng, M.; Zhou, J.; Owusu, K. A.; Mai, L.; Yu, Y. A New View of Supercapacitors: Integrated Supercapacitors. *Adv. Energy Mater.* **2019**, *9*, No. 1901081.
- (6) Shao, L.; Xu, J.; Ma, J.; Zhai, B.; Li, Y.; Xu, R.; Ma, Z.; Zhang, G.; Wang, C.; Qiu, J. MXene/RGO Composite Aerogels with Light and High-Strength for Supercapacitor Electrode Materials. *Compos. Commun.* **2020**, *19*, 108–113.
- (7) Huang, Z.; Li, L.; Wang, Y.; Zhang, C.; Liu, T. Polyaniline/Graphene Nanocomposites Towards High-Performance Supercapacitors: A Review. *Compos. Commun.* **2018**, *8*, 83–91.
- (8) Kumar, S.; Saeed, G.; Zhu, L.; Hui, K. N.; Kim, N. H.; Lee, J. H. 0D to 3D Carbon-Based Networks Combined with Pseudocapacitive Electrode Material for High Energy Density Supercapacitor: A Review. *Chem. Eng. J.* **2020**, *403*, No. 126352.
- (9) Li, C.; Wu, W.; Wang, P.; Zhou, W.; Wang, J.; Chen, Y.; Fu, L.; Zhu, Y.; Wu, Y.; Huang, W. Fabricating an Aqueous Symmetric Supercapacitor with a Stable High Working Voltage of 2 V by Using an Alkaline-Acidic Electrolyte. *Adv. Sci.* **2019**, *6*, No. 1801665.
- (10) Shao, R.; Niu, J.; Liang, J.; Liu, M.; Zhang, Z.; Dou, M.; Huang, Y.; Wang, F. Mesopore- and Macropore-Dominant Nitrogen-Doped Hierarchically Porous Carbons for High-Energy and Ultrafast Supercapacitors in Non-Aqueous Electrolytes. *ACS Appl. Mater. Interfaces* **2017**, *9*, 42797–42805.
- (11) Zhang, X.; Deng, S.; Zeng, Y.; Yu, M.; Zhong, Y.; Xia, X.; Tong, Y.; Lu, X. Oxygen Defect Modulated Titanium Niobium Oxide on Graphene Arrays: An Open-Door for High-Performance 1.4 V Symmetric Supercapacitor in Acidic Aqueous Electrolyte. *Adv. Funct. Mater.* **2018**, *28*, No. 1805618.
- (12) Yu, M.; Lu, Y.; Zheng, H.; Lu, X. New Insights into the Operating Voltage of Aqueous Supercapacitors. *Chem. - Eur. J.* **2018**, *24*, 3639–3649.
- (13) Pan, Q.; Yang, C.; Jia, Q.; Qi, W.; Wei, H.; Wang, M.; Yang, S.; Cao, B. Oxygen-Deficient $\text{BiFeO}_3\text{-NC}$ Nanoflake Anodes for Flexible Battery-Supercapacitor Hybrid Devices with High Voltage and Long-Term Stability. *Chem. Eng. J.* **2020**, *397*, No. 125524.
- (14) Wang, L.; Zhang, G.; Han, B.; Chang, Y.; Li, H.; Wang, J.; Hu, C.; Chang, Z.; Huo, Z.; Sun, X. A Two-Volt Aqueous Supercapacitor from Porous Dehalogenated Carbon. *J. Mater. Chem. A* **2017**, *5*, 6734–6739.
- (15) Zuo, W.; Xie, C.; Xu, P.; Li, Y.; Liu, J. A Novel Phase-Transformation Activation Process toward Ni-Mn-O Nanoprism Arrays for 2.4 V Ultrahigh-Voltage Aqueous Supercapacitors. *Adv. Mater.* **2017**, *29*, No. 1703463.
- (16) Zhang, K.; Lin, Y.; Chen, L.; Huang, J.; Wang, L.; Peng, M.; Tang, X.; Hu, T.; Yuan, K.; Chen, Y. Enabling 2.4-V Aqueous Supercapacitors through the Rational Design of an Integrated Electrode of Hollow Vanadium Trioxide/Carbon Nanospheres. *Sci. China Mater.* **2021**, *64*, 2163–2172.
- (17) Najib, S.; Bakan, F.; Abdullayeva, N.; Bahariqushchi, R.; Kasap, S.; Franzò, G.; Sankir, M.; Sankir, N. D.; Mirabella, S.; Erdem, E. Tailoring Morphology to Control Defect Structures in ZnO Electrodes for High-Performance Supercapacitor Devices. *Nanoscale* **2020**, *12*, 16162–16172.
- (18) Zhao, J.; Li, Z.; Yuan, X.; Yang, Z.; Zhang, M.; Meng, A.; Li, Q. A High-Energy Density Asymmetric Supercapacitor Based on Fe_2O_3 Nanoneedle Arrays and $\text{NiCo}_2\text{O}_4/\text{Ni}(\text{OH})_2$ Hybrid Nanosheet Arrays Grown on SiC Nanowire Networks as Free-Standing Advanced Electrodes. *Adv. Energy Mater.* **2018**, *8*, No. 1702787.
- (19) Li, Y.; Xu, J.; Feng, T.; Yao, Q.; Xie, J.; Xia, H. Fe_2O_3 Nanoneedles on Ultrafine Nickel Nanotube Arrays as Efficient Anode for High-Performance Asymmetric Supercapacitors. *Adv. Funct. Mater.* **2017**, *27*, No. 1606728.
- (20) Bi, W.; Wang, J.; Jahrman, E. P.; Seidler, G. T.; Gao, G.; Wu, G.; Cao, G. Interface Engineering V_2O_5 Nanofibers for High-Energy and Durable Supercapacitors. *Small* **2019**, *15*, No. 1901747.
- (21) Gao, M.; Wang, W.-K.; Rong, Q.; Jiang, J.; Zhang, Y.-J.; Yu, H.-Q. Porous ZnO-Coated Co_3O_4 Nanorod as a High-Energy-Density Supercapacitor Material. *ACS Appl. Mater. Interfaces* **2018**, *10*, 23163–23173.
- (22) Wang, S. Q.; Cai, X.; Song, Y.; Sun, X.; Liu, X. X. VO_2/MoO_3 Nanorod Composite for High-Performance Supercapacitors. *Adv. Funct. Mater.* **2018**, *28*, No. 1803901.
- (23) Liu, S.; Xu, C.; Yang, H.; Qian, G.; Hua, S.; Liu, J.; Zheng, X.; Lu, X. Atomic Modulation Triggering Improved Performance of MoO_3 Nanobelts for Fiber-Shaped Supercapacitors. *Small* **2020**, *16*, No. 1905778.
- (24) Kim, H.-S.; Cook, J. B.; Lin, H.; Ko, J. S.; Tolbert, S. H.; Ozolins, V.; Dunn, B. Oxygen Vacancies Enhance Pseudocapacitive Charge Storage Properties of MoO_{3-x} . *Nat. Mater.* **2017**, *16*, 454–460.
- (25) Hanlon, D.; Backes, C.; Higgins, T. M.; Hughes, M.; O'Neill, A.; King, P.; McEvoy, N.; Duesberg, G. S.; Mendoza Sanchez, B.; Pettersson, H.; Nicolosi, V.; Coleman, J. N. Production of Molybdenum Trioxide Nanosheets by Liquid Exfoliation and Their

Application in High-Performance Supercapacitors. *Chem. Mater.* **2014**, *26*, 1751–1763.

(26) Lee, T. H.; Pham, D. T.; Sahoo, R.; Seok, J.; Luu, T. H. T.; Lee, Y. H. High Energy Density and Enhanced Stability of Asymmetric Supercapacitors with Mesoporous MnO_2 @CNT and Nanodot MoO_3 @CNT Free-Standing Films. *Energy Storage Mater.* **2018**, *12*, 223–231.

(27) Wan, C.; Jiao, Y.; Li, J. Flexible, Highly Conductive, and Free-Standing Reduced Graphene Oxide/Polypyrrole/Cellulose Hybrid Papers for Supercapacitor Electrodes. *J. Mater. Chem. A* **2017**, *5*, 3819–3831.

(28) Liu, Y.; Li, L.; Zhu, J.; Xu, J.; Liu, S.; Wang, Y.; Zhang, C.; Liu, T. A Biomimetic *Setaria Viridis*-Inspired Electrode with Polyaniline Nanowire Arrays Aligned on MoO_3 @Polypyrrole Core-Shell Nanobelts. *J. Mater. Chem. A* **2018**, *6*, 13428–13437.

(29) Liu, Y.; Zhu, J.; Xu, J.; Liu, S.; Li, L.; Zhang, C.; Liu, T. High-Temperature Solvent-Free Sulfidation of MoO_3 Confined in a Polypyrrole Shell: MoS_2 Nanosheets Encapsulated in a Nitrogen, Sulfur Dual-Doped Carbon Nanoprism for Efficient Lithium Storage. *Nanoscale* **2018**, *10*, 7536–7543.

(30) Huang, L.; Yao, B.; Sun, J.; Gao, X.; Wu, J.; Wan, J.; Li, T.; Hu, Z.; Zhou, J. Highly Conductive and Flexible Molybdenum Oxide Nanopaper for High Volumetric Supercapacitor Electrode. *J. Mater. Chem. A* **2017**, *5*, 2897–2903.

(31) Zhang, G.; Xiong, T.; Yan, M.; He, L.; Liao, X.; He, C.; Yin, C.; Zhang, H.; Mai, L. J. N. E. α - MoO_3 -x by Plasma Etching with Improved Capacity and Stabilized Structure for Lithium Storage. *Nano Energy* **2018**, *49*, 555–563.

(32) Vasilopoulou, M.; Douvas, A. M.; Georgiadou, D. G.; Palilis, L. C.; Kennou, S.; Sygellou, L.; Soultati, A.; Kostis, I.; Papadimitropoulos, G.; Davazoglou, D.; Argitis, P. The Influence of Hydrogenation and Oxygen Vacancies on Molybdenum Oxides Work Function and Gap States for Application in Organic Optoelectronics. *J. Am. Chem. Soc.* **2012**, *134*, 16178–16187.

(33) Scanlon, D. O.; Watson, G. W.; Payne, D. J.; Atkinson, G. R.; Egde, R. G.; Law, D. S. L. Theoretical and Experimental Study of the Electronic Structures of MoO_3 and MoO_2 . *J. Phys. Chem. C* **2010**, *114*, 4636–4645.

(34) Devan, R. S.; Ho, W. D.; Chen, C. H.; Shiu, H. W.; Ho, C. H.; Cheng, C. L.; Wu, S. Y.; Liou, Y.; Ma, Y. R. High Room-Temperature Photoluminescence of One-Dimensional Ta_2O_5 Nanorod Arrays. *Nanotechnology* **2009**, *20*, No. 445708.

(35) Fic, K.; Lota, G.; Meller, M.; Frackowiak, E. Novel Insight into Neutral Medium as Electrolyte for High-Voltage Supercapacitors. *Energy Environ. Sci.* **2012**, *5*, 5842–5850.

(36) Elkholy, A. E.; Duignan, T. T.; Sun, X.; Zhao, X. S. Stable α - MoO_3 Electrode with a Widened Electrochemical Potential Window for Aqueous Electrochemical Capacitors. *ACS Appl. Energy Mater.* **2021**, *4*, 3210–3220.

(37) Li, X.; Xiang, X.; Liu, Y.; Xiao, D. Template-Free Fabrication of Hollow N-Doped Carbon Sphere (h-NCS) to Synthesize h-NCS@PANI Positive Material for MoO_3 /h-NCS@PANI Asymmetric Supercapacitor. *Appl. Surf. Sci.* **2018**, *442*, 476–486.

(38) Saeed, G.; Kumar, S.; Kim, N. H.; Lee, J. H. Fabrication of 3D Graphene-CNTs/ α - MoO_3 Hybrid Film as an Advance Electrode Material for Asymmetric Supercapacitor with Excellent Energy Density and Cycling Life. *Chem. Eng. J.* **2018**, *352*, 268–276.

(39) Shafi, P. M.; Dhanabal, R.; Chithambararaj, A.; Velmathi, S.; Bose, A. C. α - MnO_2 /h- MoO_3 Hybrid Material for High Performance Supercapacitor Electrode and Photocatalyst. *ACS Sustainable Chem. Eng.* **2017**, *5*, 4757–4770.

(40) Wang, L.; Gao, L.; Wang, J.; Shen, Y. MoO_3 Nanobelts for High-Performance Asymmetric Supercapacitor. *J. Mater. Sci.* **2019**, *54*, 13685–13693.

(41) Zhang, S.-W.; Yin, B.-S.; Liu, C.; Wang, Z.-B.; Gu, D.-M. Self-Assembling Hierarchical NiCo_2O_4 / MnO_2 Nanosheets and MoO_3 /PPy Core-Shell Heterostructured Nanobelts for Supercapacitor. *Chem. Eng. J.* **2017**, *312*, 296–305.

(42) Zhao, N.; Fan, H.; Zhang, M.; Ma, J.; Du, Z.; Yan, B.; Li, H.; Jiang, X. Simple Electrodeposition of MoO_3 Film on Carbon Cloth for High-Performance Aqueous Symmetric Supercapacitors. *Chem. Eng. J.* **2020**, *390*, No. 124477.

(43) Zheng, W.; Halim, J.; El Ghazaly, A.; Etman, A. S.; Tseng, E. N.; Persson, P. O. A.; Rosen, J.; Barsoum, M. W. Flexible Free-Standing MoO_3 / $\text{Ti}_3\text{C}_2\text{T}_z$ Mxene Composite Films with High Gravimetric and Volumetric Capacities. *Adv. Sci.* **2021**, *8*, No. 2003656.

(44) Wang, Y.; Tebyetekerwa, M.; Liu, Y.; Wang, M.; Zhu, J.; Xu, J.; Zhang, C.; Liu, T. Extremely Stretchable and Healable Ionic Conductive Hydrogels Fabricated by Surface Competitive Coordination for Human-Motion Detection. *Chem. Eng. J.* **2021**, *420*, No. 127637.

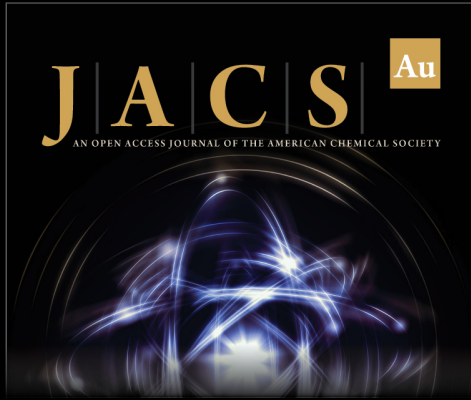
(45) Zong, W.; Lai, F.; He, G.; Feng, J.; Wang, W.; Lian, R.; Miao, Y. E.; Wang, G. C.; Parkin, I. P.; Liu, T. Sulfur-Deficient Bismuth Sulfide/Nitrogen-Doped Carbon Nanofibers as Advanced Free-Standing Electrode for Asymmetric Supercapacitors. *Small* **2018**, *14*, No. 1801562.

(46) Zhu, T.; Feng, Q.; Liu, S.; Zhang, C. Metallogel-Derived 3D Porous Carbon Nanosheet Composites as an Electrocatalyst for Oxygen Reduction Reaction. *Compos. Commun.* **2020**, *20*, No. 100376.

(47) Yang, X.; Ding, H.; Zhang, D.; Yan, X.; Lu, C.; Qin, J.; Zhang, R.; Tang, H.; Song, H. Hydrothermal Synthesis of MoO_3 Nanobelt-Graphene Composites. *Cryst. Res. Technol.* **2011**, *46*, 1195–1201.

(48) Liu, J.; Zhang, L.; Wu, H. B.; Lin, J.; Shen, Z.; Lou, X. W. D. High-Performance Flexible Asymmetric Supercapacitors Based on a New Graphene Foam/Carbon Nanotube Hybrid Film. *Energy Environ. Sci.* **2014**, *7*, 3709–3719.

(49) Cui, Y.; Zhang, J.; Jin, C.; Liu, Y.; Luo, W.; Zheng, W. Ionic Liquid-Controlled Growth of NiCo_2S_4 3D Hierarchical Hollow Nanorod Arrays on Ni Foam for Superior Performance Binder Free Hybrid Supercapacitors. *Small* **2019**, *15*, No. 1804318.



JACS Au
AN OPEN ACCESS JOURNAL OF THE AMERICAN CHEMICAL SOCIETY

Editor-in-Chief
Prof. Christopher W. Jones
Georgia Institute of Technology, USA

Open for Submissions

pubs.acs.org/jacsau

ACS Publications
Most Trusted. Most Cited. Most Read.